Supporting Material

Dynamics of Cell Shape and Forces on Micropatterned Substrates Predicted by a Cellular Potts Model

Philipp J. Albert and Ulrich S. Schwarz

Institute for Theoretical Physics and BioQuant, Heidelberg University, Philosophenweg 19, 69120 Heidelberg, Germany

A. Radius Spanning Distance Relation with Elastic Area Constraint

Many cellular Potts models (CPM) (1–3) or vertex models (4–6) for cells in tissue use an elastic (harmonic) constraint for the cell area or volume in combination with a simple line tension mediating cell-cell interaction. In addition, some models also include an elastic line tension (5, 6). For a single cell the simplest energy functional combines a simple line tension with the elastic area constraint.

$$E = \lambda_s l + k(A - A_0)^2, \tag{S1}$$

where the first term accounts for the simple line tension λ_s which scales with the cell perimeter l and the second term describes the area elasticity with elastic coefficient k and target area A_0.

As in the tension-elasticity model (TEM), the dependence of the arc radius R on the spanning distance d can be found by a force balance. First we define surface tension $\sigma = \partial E/\partial A$ and line tension $\lambda_s = \partial E/\partial l$. The surface tension pulls inwards perpendicular to the contour and the line tension exerts a force depending on the curvature of the contour. The force balance then reads

$$\sigma\vec{n} = \lambda_s \frac{\mathrm{d}\vec{t}}{\mathrm{d}l} = \lambda_s \frac{1}{R}\vec{n}, \tag{S2}$$

where the contour is parameterized by its length l, and $\vec{n}$ and $\vec{t}$ are the normal and the tangent to the contour, respectively. Calculating the derivative of Eq. (S1), Eq. (S2) becomes

$$2R(A - A_0) - \frac{\lambda_s}{k} = 0. \tag{S3}$$

This shows that the cell area A and the arc radius R are not independent of each other. In contrast to the TEM or simple-tension model (STM), the arc radius now is not controlled locally,

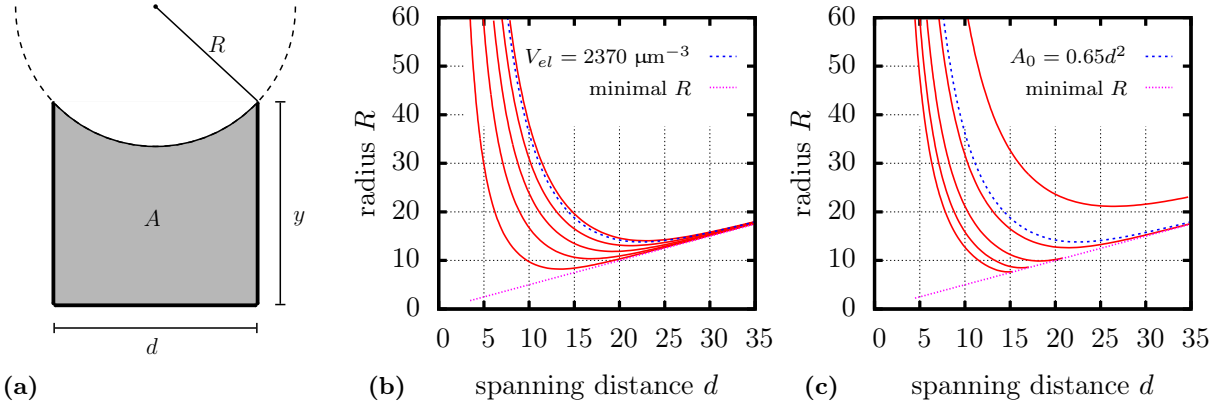

Figure S1 (a) Cell with area A confined to a U-shaped micropattern with a single circular arc. (b) $R(d)$ dependence calculated from Eq. (S4) with $V_{el} = \lambda_s/k$ increasing from 500 μm^{-3} (bottom curve) to 2500 μm^{-3} (top curve) and a target area of $A_0 = 0.65d^2$. (c) $R(d)$ dependence for a target area increasing from $A_0 = 0$ (bottom curve) to $A_0 = 0.8d^2$ (top curve) and $V_{el} = 2370\ \mu m^{-3}$. The blue dashed curves are the same in both figures with $V_{el} = 2370\ \mu m^{-3}$ and $A_0 = 0.65d^2$ both taken from (3).

but depends on the overall cell shape. Area changes at one end of the cell can influence the arc radius at the other end. For a cell on a U-shaped micropattern as depicted in Figure S1a, the implicit equation for the arc radius is found from Eq. (S3) as

$$2R\left(\frac{d}{4}\sqrt{4R^2-d^2} - R^2 \arcsin\left(\frac{1}{2}\frac{d}{R}\right) + dy - A_0\right) - \frac{\lambda_s}{k} = 0. \tag{S4}$$

As in the TEM the arc radius depends on the spanning distance d, but in addition also the height y of the U-shaped pattern influences the radius. In the following only the case of quadratic shapes with $y = d$ is considered.

There are two modes of controlling the cell shape, either by changing the target area A_0 or by changing the ratio of simple tension and the strength of the area constraint $V_{el} = \lambda_s/k$. Figure S1b shows $R(d)$ for different values of $V_{el} = \lambda_s/k$. The monotonously increasing relation between arc radius and spanning distance observed in experiments (7) can be achieved by shifting V_{el} to very small values. However, this brings the radius very close to the minimal possible radius of $R = d/2$ and such strongly invaginated cells are usually not observed experimentally. In Figure S1c the target area A_0 is changed. For small target areas Eq. (S4) does not have a solution for all spanning distances and the $R(d)$ curve ends at the minimal radius condition. Cells would collapse in such geometries. Figure S1b and S1c also show $R(d)$ (blue curves) for parameters used previously (3). Neither changing the strength $V_{el} = \lambda_s/k$ nor changing the target area A_0 can achieve a monotonously increasing relation between arc radius and spanning distance without yielding strongly invaginated cells. The addition of an elastic line tension as in the TEM to the energy functional (S1) does not change this outcome.

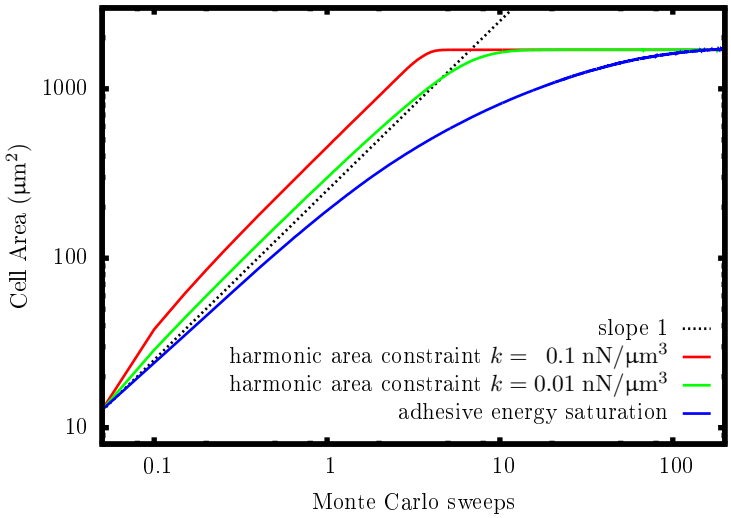

Figure S2 Cell radius during spreading as function of Monte Carlo sweeps for an elastic area constraint (see Eq. (S1)) and an saturation of the number of adhesion molecules (see Eq. (2) in the main text). The simulations are carried out with a simple line tension of $\lambda_s = 10$ nN, elastic rigidity as stated in the legend, target area $A_0 = 1700$ μm^2. For the model with saturation of adhesive energy the same parameters as for Figure 3 of the main text where used ($\sigma = 0.6$ nN, $W = 60$ nN/μm, one Monte Carlo sweep consists of 2×10^4 inversion attempts).

B. Spreading Dynamics

The spreading dynamics of a cell with an elastic area constraint as in Eq. (S1) and a cell with a saturation of the number of adhesion molecules as in Eq. 2 of the main text is expected to be different. For the former the quadratic area constraint yields a large contribution throughout the spreading process as long as cell area A and target area A_0 do not match. For the latter the energy gain from forming new adhesion contacts stays within the same order throughout the whole spreading process. This is reflected by the simulated cell area as function of Monte Carlo sweeps shown in Figure S2. For an elastic area constraint the linear area growth stops only shortly before the target area is reached. Within the Metropolis dynamics all steps increasing the cell size are accepted due to the large contribution of the area term. The growth cannot be faster than linear since only single lattice sites are inverted during each step. In a model where the cell spreads against a viscous force the area would initially grow stronger than linear. With a saturation of the adhesive energy the growth gradually slows down similar to what is seen in experiments (8, 9). Reducing the strength k of the elastic area constraint makes the transition to the steady state less abrupt, but it also results in larger fluctuations around the target area.

We also note that the limitation in adhesive area used here is similar to a limitation in membrane tension. For a cell on a homogeneously adhesive substrate the cell area and adhesive area are equal $A = A_{\mathrm{ad}}$ and no actin edge bundles exist. With the adhesive energy density

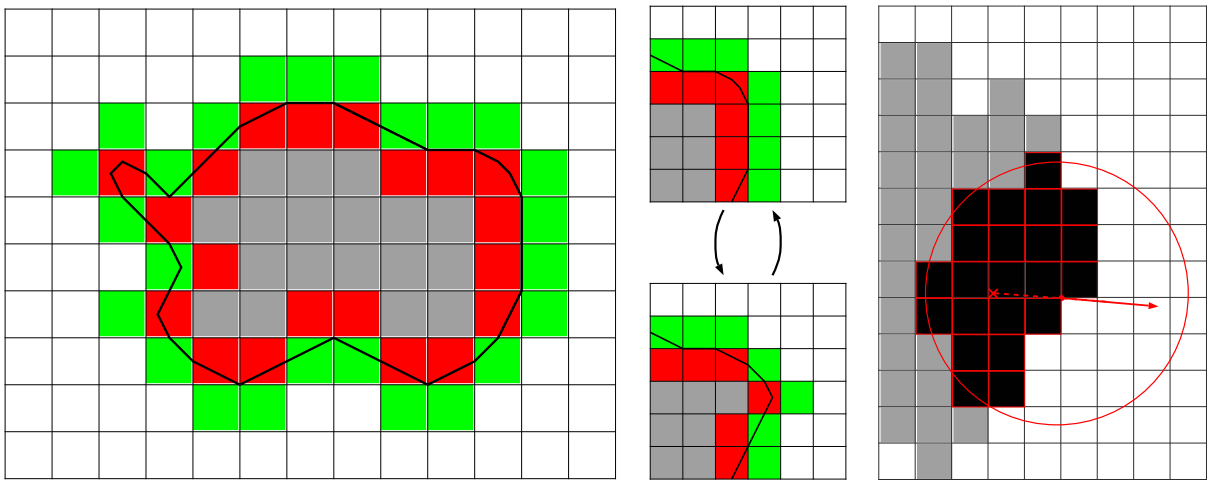

Figure S3 Cell represented on a lattice. Sites inside the cell are gray, sites in the border layer of the cell are red and sites not being occupied by the cell but in the neighborhood of border sites are green. The cell periphery is indicated by the black line. (a) Representation of a whole cell. (b) Update of a single lattice site.(c) Circular mask applied to the cell boundary to define the normal.

$W = E_0/A_{ref}$ the energy functional Eq. (2) of the main text becomes

$$\begin{aligned} E &= \lambda_s l + \sigma A - \frac{E_0}{A_{ref} + A} A \\ &= \lambda_s l + \sigma A - \frac{E_0}{A_{ref} + A} A - WA + WA \\ &= \lambda_s l + \underbrace{\left[\sigma + \frac{WA}{A_{ref} + A}\right]}_{\sigma'} A - WA \end{aligned} \tag{S5}$$

where σ' now takes the role of the surface tension. It increases with the cell area which can be interpreted as an increase due to a finite amount of membrane area. Since the energy functional stays essentially the same, the spreading dynamics and the force measurements are not directly affected by the different interpretations of the energy functional.

C. Implementation

In the lattice-based CPMs a cell is represented by a set of occupied lattice sites as illustrated in Figure S3a. Under normal conditions it is very unlikely that cells form spontaneous holes or that new part of the cell nucleate without contact to the bulk. We therefore use a modified Metropolis algorithm (2) which only allows to invert sites at the cell boundary.

The red sites in Figure S3a are occupied by the cell and form the outermost border layer of the cell. They are surrounded by the outside layer of sites (green) not occupied by the cell but being adjacent to one of the border sites. Updates by the Metropolis algorithm only happen

in these two layers. The gray lattice sites belonging to the cell bulk are passive (no holes are formed), as are the white medium sites (no nucleation away from the bulk). Occupied lattice sites can get isolated from the bulk of the cell when the cell retracts.

To define the cell boundary we use the marching square algorithm, a two-dimensional variant of the marching cube algorithm (10). Given four lattice sites the marching square algorithm defines the orientation and length of the boundary between those four sites. To calculate the contribution of a single lattice site to the cell perimeter the occupation of its eight surrounding sites needs to be known. The marching square algorithm allows only boundary orientations of $0°, 45°, 90°, \ldots$, which results in a high lattice anisotropy. The anisotropy can be reduced by allowing more possibilities for the boundary orientation and length by taking a larger neighborhood. Each occupied lattice sites gets a value assigned increasing with the number of occupied neighbors. A higher value pushes the boundary further away from this site. Similar methods to refine the marching square algorithm have been used in image processing (11). We use a square of 4x4 lattice sites to define length and orientation of the boundary between the four central sites. The boundary contribution of a single site is then defined by its 24 neighbors. The resulting cell outline is shown in Figure S3a as black line. The length of this line is used as the cell perimeter in the energy functional Eq. (2) of the main text. The cell area is defined by the number of occupied lattice sites.

Figure S3b illustrates the inversion of a lattice site. A new site is added to the green outside layer in this case. The changes required by the inversion in the red border and green outside layer are stored in a lookup table which requires knowledge about the identity of the four surrounding sites. The change in circumference calculated by the refined marching square method is also stored in a lookup table requiring the occupation values of the 24 surrounding sites.

The orientation of the normal to the cell border is found by applying a circular mask to the lattice as illustrated in Figure S3c. The vector connecting the geometrical center (cross) of the occupied lattice sites within the circle (black sites) and the circle center defines the normal direction $\vec{n}$ at the circle center. With this normal the boundary segments left and right of the original segment and their normal orientations ϕ_l and ϕ_r can be identified. The curvature is then approximated by

$$\kappa = \frac{1}{2}\frac{\phi_l - \phi_r}{l}, \tag{S6}$$

where l is the length of the boundary segment. The factor $1/2$ arises from two boundary segments sharing one kink in the boundary.

D. Reconstruction of Traction Force from Simulated Force Fields

As described in the main text, the simulated traction force is used to calculate a displacement field from which the traction can be reconstructed with the Fourier-transform traction cytometry method (12) to make it comparable to experimental results. First, the cell shape is obtained as shown in Figure S4a. Due to the finite simulation temperature the membrane fluctuates

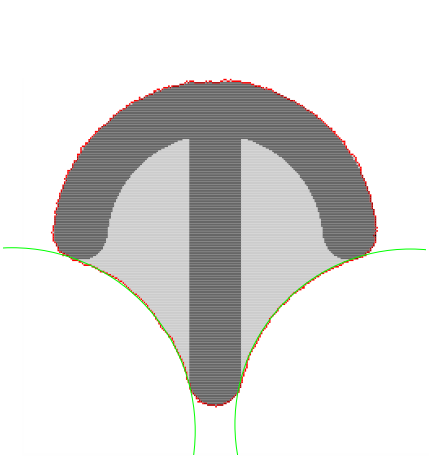

a Cell shape

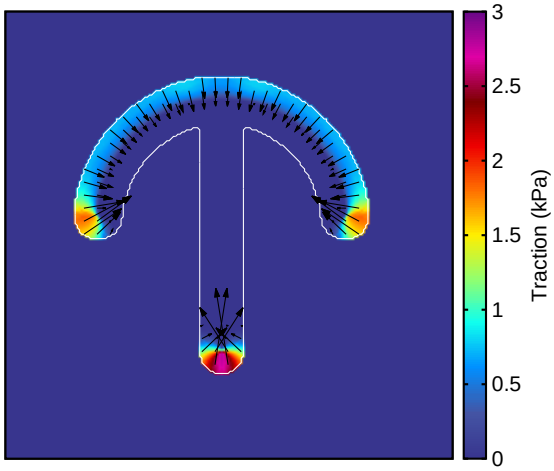

b Traction force in contour

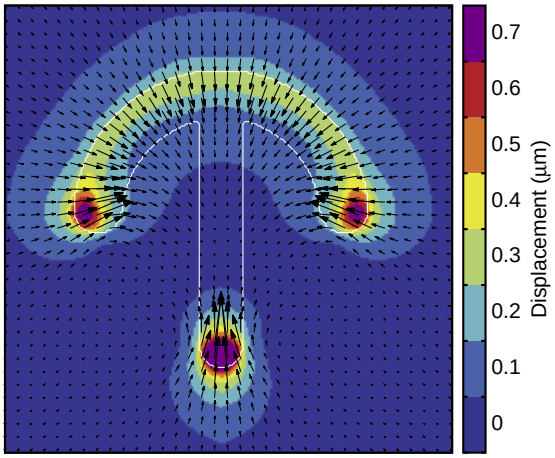

c Displacement field

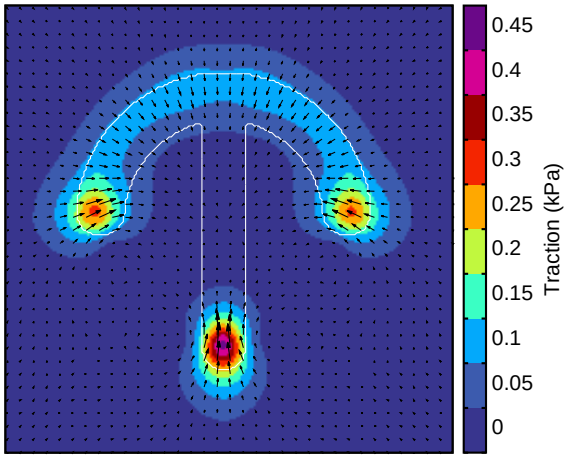

d Reconstructed traction field

Figure S4 Different stages of the reconstruction of traction forces from the CPM.

and the traction force in the cell contour is obtained by averaging over 2×10^5 Monte Carlo sweeps. The traction force is distributed over a 2 µm wide stripe beneath the membrane. To be more precise, we apply a disk shaped kernel with a radius of 2 µm to each lattice site distributing the forces to the surrounding sites. In combinations with a pattern-shaped kernel it is ensured that traction forces are only applied to adhesive parts of the patterns and that forces from membrane fluctuation above non-adhesive parts are propagated to the pattern. Both magnitude and vector field of the traction force are shown in Figure S4b. Figure S4c shows the displacement field found by our finite element method for the traction field in Figure S4b on a substrate with Young modulus of 5 kPa. From the displacement field the traction force is reconstructed with the Fourier-transform traction cytometry method with a regularization parameter of $3 \times 10^{-8} \mu m^2/Pa^2$ arriving at the final result shown in Figure S4d. Our choice of the regularization parameter yields the same total traction before and after reconstruction.

Supporting References

1. Graner, F., and J. Glazier, 1992. Simulation of biological cell sorting using a two-dimensional extended Potts model. *Phys. Rev. Lett.* 69:2013–2016.

2. Glazier, J., and F. Graner, 1993. Simulation of the differential adhesion driven rearrangement of biological cells. *Phys. Rev. E* 47:2128.

3. Vianay, B., J. Käfer, E. Planus, M. Block, F. Graner, and H. Guillou, 2010. Single Cells Spreading on a Protein Lattice Adopt an Energy Minimizing Shape. *Phys. Rev. Lett.* 105:3–6.

4. Hufnagel, L., A. a. Teleman, H. Rouault, S. M. Cohen, and B. I. Shraiman, 2007. On the mechanism of wing size determination in fly development. *Proc. Natl. Acad. Sci. U. S. A.* 104:3835–40.

5. Farhadifar, R., J.-C. Röper, B. Aigouy, S. Eaton, and F. Jülicher, 2007. The influence of cell mechanics, cell-cell interactions, and proliferation on epithelial packing. *Curr. Biol.* 17:2095–104.

6. Käfer, J., T. Hayashi, A. F. M. Marée, R. W. Carthew, and F. Graner, 2007. Cell adhesion and cortex contractility determine cell patterning in the Drosophila retina. *Proc. Natl. Acad. Sci. U. S. A.* 104:18549–18554.

7. Bischofs, I. B., F. Klein, D. Lehnert, M. Bastmeyer, and U. S. Schwarz, 2008. Filamentous network mechanics and active contractility determine cell and tissue shape. *Biophys. J.* 95:3488–3496.

8. Gauthier, N. C., M. A. Fardin, P. Roca-Cusachs, and M. P. Sheetz, 2011. Temporary increase in plasma membrane tension coordinates the activation of exocytosis and contraction during cell spreading. *Proc. Natl. Acad. Sci. U. S. A.* 108:14467–72.

9. Cuvelier, D., M. Théry, Y.-S. Chu, S. Dufour, J.-P. Thiéry, M. Bornens, P. Nassoy, and L. Mahadevan, 2007. The universal dynamics of cell spreading. *Curr. Biol.* 17:694–9.

10. Lorensen, W., and H. Cline, 1987. Marching cubes: A high resolution 3D surface construction algorithm. *In* ACM Siggraph Comput. Graph. ACM, volume 21, 163–169.

11. Mantz, H., K. Jacobs, and K. Mecke, 2008. Utilizing Minkowski functionals for image analysis: a marching square algorithm. *J. Stat. Mech. Theory Exp.* 2008:P12015.

12. Sabass, B., M. L. Gardel, C. M. Waterman, and U. S. Schwarz, 2008. High resolution traction force microscopy based on experimental and computational advances. *Biophys. J.* 94:207–20.